Observation of quantum oscillations in the extreme weak anharmonic limit

A. Théry [1], B. Neukelmance [1], B. Hue [1], W. Legrand [1], L. Jarjat [1], J. Craquelin [1], M. Villiers,[1]
A. Cottet [1,2], M. R. Delbecq [1,2,3], and T. Kontos [1,2,*]

[1] *Laboratoire de Physique de l'École Normale Supérieure, ENS, Université PSL, CNRS, Sorbonne Université,*
Université Paris-Diderot, Sorbonne Paris Cité, Paris, France
[2] *Laboratoire de Physique et d'Etude des Matériaux, ESPCI Paris, PSL University, CNRS, Sorbonne Université, Paris, France*
[3] *Institut universitaire de France (IUF)*

We investigate a granular aluminium quantum circuit with an anharmonicity of the order of its decoherence rate in a three-dimensional microwave cavity. We perform single qubitlike manipulations such as Rabi oscillations and Ramsey fringes. Our findings, supported by quantitative numerical modeling, show that a very weakly anharmonic oscillator can also display quantum oscillations outside the qubit regime. These oscillations are hard to disambiguate from qubit oscillations in time domain measurements for a single driving frequency. This sheds light on recent findings for material superconducting quantum bits. Our platform shows in addition large magnetic field resilience which could find applications for quantum enhanced dark matter search.

Superconducting circuits have become a major platform for quantum information processing and quantum amplification. Whereas the conventional Josephson junction has been extensively used so far, many efforts aim to replace it by more elaborate materials which range from semiconducting nanowires [1] or nanotubes [2] to 2D materials [3–5]. Such setups would offer an enhanced electrical tunability (via, e.g., gate electrodes) and magnetic field resilience. Both these aspects could be crucial regarding new applications for quantum sensing or for scaling up quantum information processing platforms [3–5]. In particular, the potential for quantum sensing applications range from quantum amplification of cosmological signals to readout of topological systems.

These new platforms are appealing in terms of technology, but they often display a reduced anharmonicity which could endanger their qubit character. This motivates the detailed study of the dynamics of such systems at the frontier between the harmonic and the anharmonic regime, i.e., when the anharmonicity is comparable to the damping rate of these oscillators. In this context, the use of a simple superconducting material offering both low anharmonicity and weak losses without the inherent complexity of low dimensional materials would be appealing. Granular aluminium (grAl) is such a material. It can be used both in the extreme weak anharmonic regime and in the qubit regime [6,7,10–12]. It is therefore ideal to study the above mentioned crossover.

In this work, we use a grAl based quantum circuit in the extreme weak anharmonic regime. We show that we can perform qubitlike manipulations, such as Rabi oscillations and Ramsey interferometry. However, the dynamics of the circuit involve many oscillator levels. This behavior is understood quantitatively by a simple quantum model of an anharmonic oscillator. By the analysis of the Rabi chevron patterns and the Ramsey fringes, we can assess about the "quantumness" of the observed oscillations. We show in particular that single time domain traces in these systems can easily mimic qubit dynamics both for Rabi and Ramsey oscillations. This emphasizes that one has to be cautious in assigning these qubitlike signals to a qubit signature. Doing so, we benchmark the time domain oscillations in the weak anharmonic regime. In addition, we are able to drive our circuit up to 0.7 T making our simple grAl circuit appealing for magnetic field resilient quantum sensing applications.

The Josephson junction is mounted in a copper three-dimensional (3D) microwave cavity with a fundamental frequency of about $\omega_{cav} = 2\pi \times 6.0$ GHz and a quality factor $Q = 2700$ at low temperature. The whole setup is mounted in a dilution refrigerator with a standard microwave setup [8] and all the measurements are carried out at $T \approx 20$ mK. Such a geometry is that of a "3D-transmon" [9,10]. The details of the nanofabrication are given in the Appendix. From the DC switching current measurements, we estimate the supercurrent as shown in [13] to $I_c \approx 600$ nA(see Appendix). The inducance of the circuit is estimated to $L_J \approx 1.63$ nH from the Mattis-Bardeen formula [10]. From microwave simulations, we estimate for the layout of Fig. 1, which yields a charging energy of $E_C \approx 47$ MHz, which yields a resonance frequency of 6.14 GHz, close to our measurements. In addition, from the DC measurements stated above, we can expect a transmon anharmonicity of $K_0 \approx \mathcal{C}\pi a \omega_1^2 / j_c V_{grAl} \approx 250$ kHz, with $\mathcal{C} = 3/16$ and $a = 5$ nm [10,12], a being the Al grain size. The parameters of our circuit can be determined experimentally by the microwave two-tone spectroscopy which is shown in Fig. 1(c), detuned from the cavity mode. We observe a clear dip at 5.9102 GHz which displays the characteristic asymmetric lineshape of an anharmonic oscillator as the power of the microwave input signal is increased. The linewidth at lowest power is $\Gamma_{exp} \approx 2\pi \times 0.935$ MHz ± 0.1 MHz, as fitted by the black line. From the shift toward low frequencies of

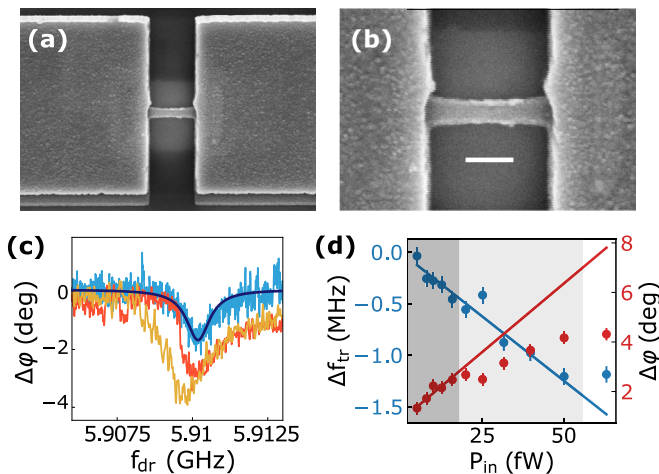*Corresponding author: takis.kontos@ens.fr

FIG. 1. (a) Large scale view of the grAl transmon circuit. (b) Micrograph of the grAl Josephson inductor. The bar is 250 nm. (c) Microwave spectroscopy of the grAl circuit for −113 dBm (blue), −101 dBm (red), and −97 dBm (orange). It shows the characteristic features of an anharmonic oscillator. (d) From the power dependence of the phase contrast and the grAl circuit frequency, we extract an anharmonicity of ≈ 250 kHz. The shaded dark gray region is the linear regime from which we extract these values. In this region, we can compute the excitation number of the device. We find that the device remains in the linear regime up to an average occupation number around two.
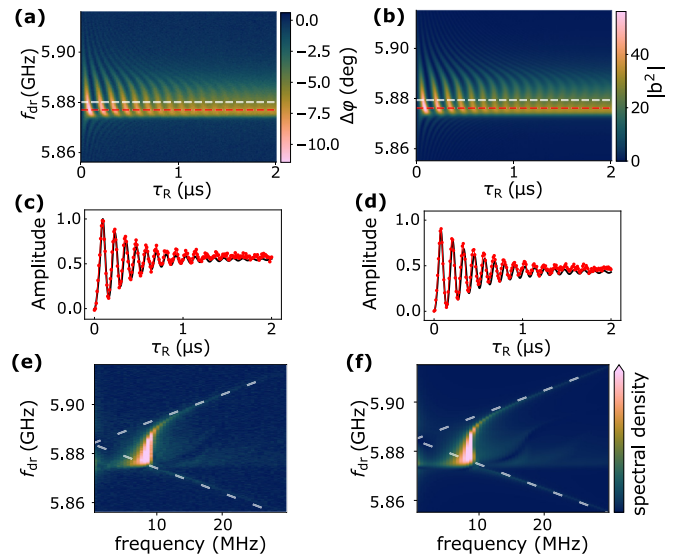

FIG. 2. (a) Rabi chevrons of the grAl transmon at $B = 0$ T as observed from the phase of the cavity signal at $f_R = 6.0$ GHz. (b) Modeling of the Rabi chevrons for $K = -2\pi \times 200$ kHz and $\Gamma = 2\pi \times 0.954$ MHz and a Hilbert space truncated at 120 quanta. The driving frequency is fixed using the frequency of the maximum dephasing of the measured chevron. (c) Measurement (red dots) and modeling (black lines) for the Rabi-like damped oscillations of the grAl transmon for the red cuts represented in panels (a) and (b). (d) Measurement (red dots) and modeling (black lines) for the Rabi-like damped oscillations of the grAl transmon for the white cuts represented in panels (a) and (b). (e) Experimental Fourier transform of the Rabi chevrons showing the spectral content of the observed oscillations. (f) Modeling of the Fourier transform of the Rabi chevrons showing good agreement with the experiment.

the edge of the transmon resonance and the phase contrast as the power is increased, shown in Fig. 1(d), we calibrate the microwave power and estimate a Kerr anharmonicity of about $K_{\mathrm{exp}} \approx 2\pi \times 250$ kHz and a coupling between the cavity and the transmon of about $g \approx 16$ MHz. Details on this calculation can be found in Appendixes B and C. This is in good agreement with the expected anharmonicity given the inherent uncertainty on the grain size of the GrAl. The linewidth observed at lowest power is directly related to the decoherence rate of the circuit. This places our circuit in the regime of extreme weak anharmonicity where $K_{\mathrm{exp}} \lesssim \Gamma_{\mathrm{exp}}$. Does this regime enable quantum oscillations such as Rabi-like oscillations and Ramsey fringes which are usual signatures of driven quantum systems? This question is addressed in the subsequent part of the paper.

We first study Rabi oscillations as a function of the time τ_R of the excitation burst and the carrier frequency, f_{dr}, at zero external magnetic field B [see Fig. 2(a)]. The state of the circuit is measured using the conventional dispersive readout, i.e. the phase φ of the microwave signal at the cavity resonance frequency $f_{\mathrm{cav}} = 6.0$ GHz here. The phase contrast $\Delta\varphi$ is simply related to the population of the circuit via $\Delta\varphi = 2\chi \langle \hat{b}^{\dagger}\hat{b} \rangle / \kappa$ where χ is the cross-Kerr coupling between the cavity photons and the circuit, κ is the cavity linewidth, and $\hat{b}$ is the transmon annihilation operator of the weakly anharmonic oscillator picture for our circuit. Defining g as the circuit-cavity coupling strength, we have $\chi = -2Kg^2/(f_{\mathrm{cav}} - f_0)^2$. The specific power of the drive and the cavity readout pulses are respectively $P_{dr} = -78$ dBm and $P_{\mathrm{cav}} = -103$ dBm. As explained above, the phase contrast is a direct measurement of $\langle \hat{b}^{\dagger}\hat{b} \rangle$. As shown in Fig. 2(a),

we observe the characteristic fringes witnessing Rabi oscillations for conventional qubits. Nevertheless, we should stress that this is a different regime from the qubit regime. This is first qualitatively shown by the observed unusual "Rabi chevron" pattern. Two features are particularly striking: first, the "chevron pattern" seems truncated below the continuous wave resonance frequency; second, a closer inspection of the oscillations shows that they are nonsinusoidal. Interestingly, the asymmetry can be qualitatively recovered by stating that, similarly to the two level system case, the chevrons result from a multiplication of the frequency envelope of the transition and the time domain damped Rabi oscillations. In such a heuristic picture, the asymmetry stems simply from the asymmetry of the lineshape of a Duffing oscillator.

It is possible to numerically model the dynamics of the circuit using as input parameters K, Γ, and the driving amplitude of the circuit thanks to the Qutip Python package. The simulation is run in the rotating frame by varying the detuning Δf_{dr} between the drive and ω_0. The result of such a simulation is shown in Fig. 2(b), where the driving frequency has been fixed using the frequency of the point with maximum contrast in the experiment. We find an excellent agreement with the data for $K = -2\pi \times 200$ kHz and $\Gamma = -2\pi \times 0.954$ MHz. These values are close to those determined independently by the continuous wave spectroscopy of the circuit in Fig. 1(c). Interestingly, the population $\langle \hat{b}^{\dagger}\hat{b} \rangle$ of the transmon which is
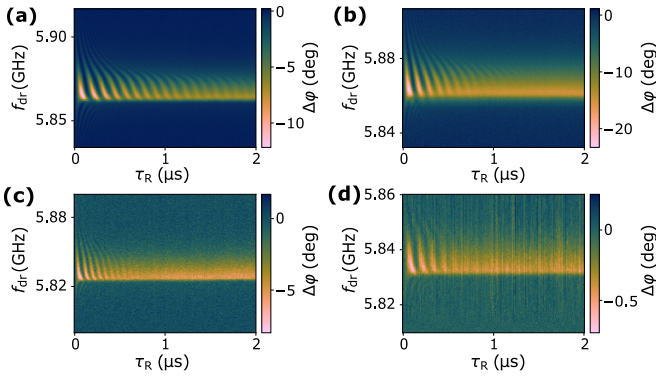
FIG. 3. (a) Rabi chevrons of the grAl transmon at $B = 0.15$ T (b) Rabi chevrons of the grAl transmon at $B = 0.45$ T (c) Rabi chevrons of the grAl transmon at $B = 0.6$ T (d) Rabi chevrons of the grAl transmon at $B = 0.7$ T.

encoded in the phase contrast is found to oscillate between nearly 0 to about 60. This shows that we are not in a qubit regime, although we can observe quantum oscillations of the state of our circuit. The agreement between the modeling and the data is further exemplified in Figs. 2(c) and 2(d). In order to further test the validity of the numerical simulation for modeling our circuit, it is interesting to Fourier transform the time domain signals. This is shown in Figs. 2(e) and 2(f) (for the experiment and the theory, respectively). We observe again an excellent agreement and all the features observed experimentally are observed in the modeling. In particular, we identify a linear behavior at large positive or negative detuning. This is a sinusoidal regime with a simple broadening arising from the decay rate of the circuit. In addition, the general features are strongly asymmetric in the detuning (vertical) axis. Such a behavior is not expected for a spin 1/2 or a conventional transmon qubit as it should be symmetric and scale like $\Omega_{\text{qubit}} = \sqrt{\Omega_0^2 + (\omega_{dr} - \omega_0)^2}$, where $\omega_{dr} = 2\pi f_{dr}$ and Ω_0 is a linear function of the drive amplitude δ. This is one important qualitative difference with our circuit. Close to 5.88 GHz, we observe a broad feature in the spectrum indicating a nonsinusoidal behavior. Rabi-like oscillations are observed here in a regime totally different than conventional qubits.

The observed "Rabi chevron" pattern is specific to the weakly anharmonic regime. It is interesting to put our findings in perspective with recent works using, e.g., 2D material as a weak link for replacing the Josephson junction [3–5]. In Ref. [4] in particular, there is a striking similarity of the observed "Rabi chevron" patterns with Fig. 2(a). The immediate consequence of our findings is that it seems difficult to distinguish between the extreme weak anharmonic regime and the qubit regime simply by measuring individual time-domain cuts at a given detuning. We will see below that this holds true even if Ramsey-like fringes are observed.

The fact that the superconducting reservoirs are made of Nb, which has a rather high critical field, combined by the magnetic field resilience of GrAl films makes it possible to operate our superconducting circuits at high magnetic field. This is shown in Fig. 3. Each of the panels corresponds to a different magnetic field ranging from 0.15 T to 0.7 T. Whereas

the Rabi chevrons are barely affected at 0.15 T, they are more affected at 0.7 T, but still clearly visible. The decoherence time decreases from $T_{\text{Rabi}} \approx 1.25\,\mu\text{s}$ to $T_{\text{Rabi}} \approx 0.3\,\mu\text{s}$. We attribute this decrease to the slight misalignment between the B-field axis and the plane of the quantum circuit. Interestingly, we find a B-field resilience up to 0.2 T in out of plane b-field (see Appendix [14]). This is about two orders of magnitude larger than conventional superconducting qubits or grAl based resonators [15].

How quantum are our observed oscillations if we are not in a qubit limit? This question echoes with the old debate on whether a weak anharmonic oscillator displaying Rabi oscillations can at all be considered as a quantum system or not [16–18]. In our case, the Rabi chevron pattern is a strong discriminator between the classical and the quantum model which has an excellent agreement with our experiment. In particular, we can compare the expected frequency content between the two models. In the classical model, a single Rabi frequency is expected $\Omega_{cla} = \mathcal{A}(\delta)|\omega_{dr} - \omega_0|$, with $\mathcal{A}(\delta)$ a sublinear function of the driving amplitude a. Such an expression contrasts with the qubit case Ω_{qubit} which contains, in addition, a "transverse Rabi field" arising from the driving of the effective two level system in the rotating frame. The expression of Ω_{cla} means that we should expect only two symmetric lines in the maps 2(e) and 2(f). While at large detuning around 5.87 GHz or 5.90 GHz a linear dispersion is present, this is clearly not the case at low detuning both in terms of frequency content and dispersion, as highlighted by the dashed lines in Figs. 2(e) and 2(f). Thus, our findings are not explained by the classical anharmonic model. This further validates that we observe quantum oscillations in the time domain manipulation of our transmon circuit.

The final picture for the dynamics of our system can be sketched by performing Ramsey interferometry. A first pulse of duration $\tau_0 = 30$ ns with $P_{dr} = -78$ dBm is followed by a waiting time τ_{Ramsey}, by a second τ_0 with $P_{dr} = -78$ dBm, and by a readout pulse. As in the conventional Ramsey interferometry setup, they correspond to half of one modulation in the Rabi sequence between the low and high number of quanta in Fig. 2(c). As shown in the 2D map of Fig. 4(a), we observe fringes which are the result of Ramsey interferences taking place in our circuit. Ramsey fringes are slightly asymmetrical, however, whereas there was a clear qualitative difference between the observed Rabi chevron pattern and that expected for a qubit, the asymmetry in the Ramsey fringes is not as noticeable. The difference in frequency between the Rabi chevrons of Fig. 2 and the Ramsey fringes is due to a slight shift of the circuit frequency. The simulation of this experiment is shown in Fig. 4(b). The duration of the pulses is 31 ns. The parameters are the same as in the Rabi chevrons simulation of Fig. 2, and the frequency offset is again set using the point of maximum contrast in the measurement. As for the Rabi chevrons, the modeling of the Ramsey interferometry reproduces closely the behavior of the device. Ramsey oscillations after a pulse $\pi/2$ are shown in 2(b) for the measurement and the simulation. The frequency and length of the pulses are 5.91 GHz and 20 ns for the measurement, and 5.9106 GHz and 21 ns in the simulation. We find an excellent agreement between the two curves. This agreement is also shown for time traces in Fig. 4(c). As in the Rabi oscillations, they differ
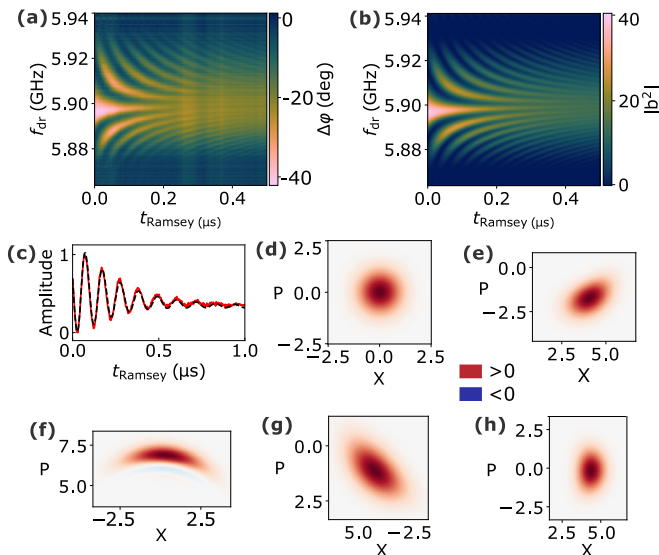
FIG. 4. (a) Ramsey fringes as a function of detuning and time delay between the two "$\pi/2$" pulse of duration τ_0. (b) Simulated Ramsey fringes for the same parameters as in Fig. 2 and a Hilbert space truncated at 80 quanta. The duration of the $\pi/2$ pulses is 31 ns. The frequency is defined relatively to the measurement frequency. (c) Measurement (red) and modeling (black) for the Ramsey interferometry of the grAl transmon after a $\pi/2$ pulse. The measurement pulse is 20 ns long at a frequency of 5.91 GHz, the simulation pulse is 21 ns long at 5.9016 GHz. (d), (e), (f), (g), (h) Simulated Wigner tomography for our parameters and $f_{dr} = 5.9188$ GHz for $t_{\text{pulse}} = 0, \tau_0, 2\tau_0, 3\tau_0, 70\tau_0$.

from the sinusoidal oscillations expected for Ramsey fringes in a two level system. We are led to conclude that the Rabi chevron pattern is more discriminant for disambiguating the qubit and the weak anharmonic regime, although the quantitative analysis of both fringes reveals strong difference with the qubit case. Since we find a very good agreement between the modeling and our experimental findings, it is interesting to further simulate the Wigner tomography expected for different pulse times of our weakly anharmonic oscillator. Such a result is shown in Figs. 4(c)–4(f). We show the Wigner functions for pulse times $t_{\text{pulse}} = 0, \tau_0, 2\tau_0, 3\tau_0, 70\tau_0$. Except from the starting point in vacuum, we see that there are clear signatures of nonclassicality in the form of squeezing and negative parts in the Wigner tomography. Interestingly, the $2\tau_0$ leads to the most nonclassical state as it displays negative, forming a blue crescent in the Wigner function whereas τ_0 displays simple squeezing. This is also a strong difference with the qubit case. In our system, the pulse time τ_0 does not play a special role, like for a qubit.

As a conclusion, we have investigated a simple superconducting circuit made out of a granular aluminium Josephson junction in the time domain. We observe quantum oscillations, i.e., Rabi oscillations and Ramsey fringes. We have a quantitative understanding of the Rabi oscillations in the extreme weak anharmonic regime and the Ramsey fringes are qualitatively similar to the qubit regime. Although our quantum circuit is not a quantum bit, it displays all the requested features for quantum sensing and quantum amplification. In particular, we could in principle use it in the photon number
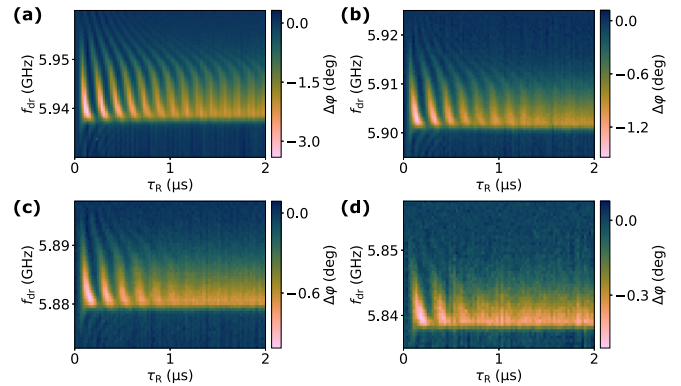
resolved regime to use it as a single photon detector. Such detectors have been put forward recently for quantum sensing of cosmological objects using conventional transmon qubits. However, a major hurdle for the use of these single photon detectors is magnetic field resilience. For example, there is a strong motivation to sense single microwave photon for quantum enhanced axion dark matter search [19] in cavities in strong magnetic field. Our quantum circuit could therefore have interesting applications for quantum sensing of cosmological signals.

FIG. 5. Rabi chevrons of the grAl transmon for out of plane B fields. (a) $B = 0$ T, (b) $B = 0.1$ T, (c) $B = 0.15$ T, and (d) $B = 0.2$ T.

APPENDIX A: RABI OSCILLATIONS WITH OUT OF PLANE MAGNETIC FIELD AND WITH DIFFERENT DRIVE AMPLITUDES

In the main text, we have shown magnetic field resilience for an in-plane magnetic field up to 0.7 T. It is interesting to explore the same feature for an out-of-plane magnetic field. In addition to the Rabi measurements made with an in-plane magnetic field, we show that our device is strongly resilient to out-of-plane magnetic field. Figure 5 shows Rabi chevrons observed for magnetic fields perpendicular to the device plane, ranging from 0 to 0.2 T. This is roughly two orders of magnitude more than the expected mT range for magnetic field resilience of plain Al grAl material [15].

We also present in this section the amplitude dependence of the measured Rabi oscillations. As expected since we do not have a simple two-level system, the extracted Rabi frequency does not scale linearly with the amplitude of excitation in the cavity (see Fig. 6).

APPENDIX B: NANOFABRICATION AND DC CHARACTERIZATION OF OUR GRAL JOSEPHSON JUNCTIONS

Our granular aluminium (grAl) transmon is fabricated in a single nanolithography step using two evaporation angles.
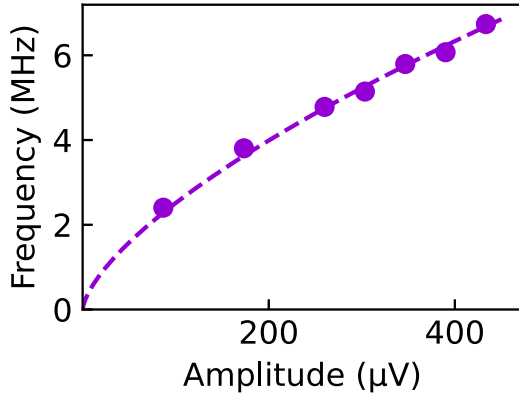
FIG. 6. Amplitude dependence of the Rabi frequency.

These evaporations are done in an evaporator with a base pressure of 5×10^{-10} mbar. First, a layer of 30 nm Al is evaporated at a rate of 1.9 Å/s with an oxygen pressure of 1.2×10^{-5} mbar at a normal angle. Second, a Nb layer of 50 nm is evaporated with an angle of $45°$. This recipe is similar to the one of the Karlsruhe group [6]. The lithography layout is essentially composed of two antenna pads of dimensions $500 \, \mu m \times 250 \, \mu m$ separated by $20 \, \mu m$ as shown in Fig. 1(a). The grAl Josephson junction is shown in Fig. 1(b). The junction dimensions are $500 \, nm \times 100 \, nm \times 30 \, nm$. The junction sheet resistance obtained with our recipe is about 1 kΩ at room temperature. The device presented in this paper has a junction resistance of 6.2 kΩ at room temperature. These devices are characterized at low temperatures ($T = 20$ mK) using either a vector network analyzer or a SHFQC (Zurich Instruments). Using a DC setup, we measure a Josephson supercurrent $I_c \lesssim 600$ nA, yielding an $I_c R_n \approx 5$ mV and a supercurrent density $j_c \approx 0.25 \, mA/\mu m^2$. Interestingly, the critical current only decreases by about 10% at a magnetic field of 2 T. We show in this section the I(V) curve which we measure on a typical grAl Josephson junction. As we see in Fig. 7, the I(V) curve is hysteretic and the switching current is about 600 nA. As shown in Ref. [13], the switching current is a good estimate of the critical current even for such small values. The inductance of the circuit is estimated using the Mattis-Bardeen theory as in [10]:
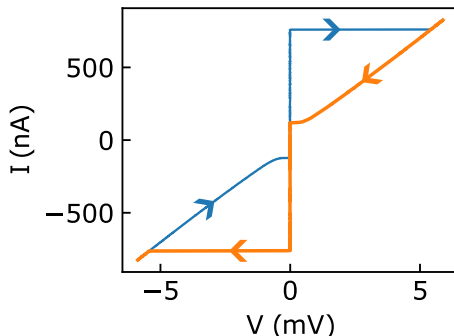
$$L_J = \frac{\hbar R_n}{\pi \Delta}, \tag{B1}$$

FIG. 7. I(V) curve of our grAl Josephson junctions.

where R_n is the normal state resistance and Δ the superconducting gap. In our case, we use $R_n = 6.2 k\Omega$ and $\Delta = 800 \, \mu eV$. The latter corresponds to the estimated proximitized value for the gap in Nb/Al planar structures [20].

APPENDIX C: DERIVATION OF THE COUPLING CONSTANT BETWEEN THE QUANTUM CIRCUIT AND THE CAVITY

We show here the details of the derivation for the coupling constant between the cavity and the circuit. We also give the relationship between the excitation number of the quantum circuit and the power of the drive sent in the cavity. We consider a quantum circuit of angular frequency ω_0, coupled to a cavity mode of angular frequency ω_r. $\Delta = \omega_0 - \omega_r$ is the detuning between the cavity and the quantum circuit. We only consider the Kerr anharmonicity of the circuit, which is true at low excitation levels where higher order anharmonicity can be neglected. The Hamiltonian of the system is

$$\hat{H} = \hbar \omega_r \hat{a}^\dagger \hat{a} + \hbar \omega_0 \hat{b}^\dagger \hat{b} + g(\hat{a}^\dagger \hat{b} + \hat{b}^\dagger \hat{a}) - \hbar \frac{K}{2} \hat{b}^\dagger \hat{b}^\dagger \hat{b} \hat{b}, \tag{C1}$$

where $\hat{a}$ and $\hat{b}$ are the annihilation operators of the cavity mode and the quantum circuit, respectively. This Hamiltonian can be diagonalized using a Bogoliubov transformation, as done in [21]:

$$\hat{H}_{\text{disp}} = \hbar \tilde{\omega}_r \hat{a}^\dagger \hat{a} + \hbar \tilde{\omega}_0 \hat{b}^\dagger \hat{b} + \frac{\hbar K_a}{2} \hat{a}^\dagger \hat{a}^\dagger \hat{a} \hat{a}$$
$$- \frac{\hbar \tilde{K}}{2} \hat{b}^\dagger \hat{b}^\dagger \hat{b} \hat{b} + \hbar \chi_{ab} \hat{a}^\dagger \hat{a} \hat{b}^\dagger \hat{b}, \tag{C2}$$

where

$$\tilde{\omega}_r = \frac{1}{2}(\omega_r + \omega_0 - \sqrt{\Delta^2 + 4g^2}), \tag{C3a}$$

$$\tilde{\omega}_0 = \frac{1}{2}(\omega_r + \omega_0 + \sqrt{\Delta^2 + 4g^2}), \tag{C3b}$$

$$K_a \simeq -\frac{E_c}{\hbar}\left(\frac{g}{\Delta}\right)^4, \quad \tilde{K} \simeq K, \quad \chi_{ab} \simeq -2\frac{g^2 K}{\Delta(\Delta - K)}, \tag{C4}$$

where K_a and $\tilde{K}$ are self-Kerr nonlinearities, and χ_{ab} is a cross-Kerr interaction between the cavity and the circuit. The cross-Kerr enables the readout of the circuit by shifting the cavity frequency by $\Delta \omega_r = \chi_{ab} \langle b^\dagger b \rangle$, where $\langle b^\dagger b \rangle$ is the average occupation level of the circuit. This frequency shift results in a phase shift of the cavity mode: $\Delta \varphi = \arctan(\frac{2\Delta \omega_r}{\kappa}) \sim \frac{2\Delta \omega_r}{\kappa}$, where κ is the linewidth of the cavity, and $\kappa \ll \Delta$. Thus,

$$\Delta \varphi = 2\frac{\chi_{ab}}{\kappa} \langle b^\dagger b \rangle. \tag{C5}$$

The self-Kerr results in a shift of the quantum circuit frequency

$$\Delta \omega = -K \langle b^\dagger b \rangle. \tag{C6}$$

Equations (C5) and (C6) show that at low enough excitation number, the cavity phase shift, and the circuit frequency shift are linear with the excitation number. We deduce the coupling constant g by measuring these two quantities in this

linear regime:

$$g = \frac{\Delta}{2}\sqrt{\left|\frac{\Delta\varphi\kappa}{\Delta\omega}\right|}. \tag{C7}$$

Using the parameters of our device $\Delta = 2\pi \times 80\,\text{MHz}$, $\kappa = 2\pi \times 2.2\,\text{MHz}$ and fits of $\Delta\phi$ and $\Delta\omega$, shown in Fig. 1, we find $g = 17\,\text{MHz}$.

APPENDIX D: DERIVATION OF THE EXCITATION NUMBER IN THE QUANTUM CIRCUIT

We derive the average excitation number $\langle b^\dagger b\rangle$ of the anharmonic oscillator when a signal of angular frequency ω_{RF} is sent through the cavity. We consider the Hamiltonian given in Eq. (C1):

$$\hat{H} = \hbar\omega_r\hat{a}^\dagger\hat{a} + \hbar\omega_0\hat{b}^\dagger\hat{b} + \hbar g(\hat{a}^\dagger\hat{b} + \hat{b}^\dagger\hat{a}) - \hbar\frac{K}{2}\hat{b}^\dagger\hat{b}^\dagger\hat{b}\hat{b}. \tag{D1}$$

We derive the equation of motion of $\hat{a}$ and $\hat{b}$ using the input-output formalism. A more detailed presentation of this formalism can be found in Ref. [21]. The cavity is coupled to the input and output lines via two ports of equal coupling constants κ_p. A drive signal is sent through the input port at angular frequency ω_{RF}. The drive is described by a source term $\hat{b}_{\text{in}}(t)$, defined so that the power sent at the input port is $P_{\text{in}}(t) = \hbar\omega_{\text{RF}}\langle\hat{b}^\dagger_{\text{in}(t)}\hat{b}_{\text{in}}(t)\rangle$. Internal losses of the cavity are taken into account as a third port of coupling constant κ_0. The total decay rate of the cavity is then $\kappa = 2\kappa_p + \kappa_0$. The equation of motion of $\hat{a}$ is given by

$$\frac{d}{dt}\hat{a}(t) = \frac{i}{\hbar}[\hat{H}, \hat{a}] - \frac{\kappa}{2}\hat{a}(t) - \sqrt{\kappa_p}\hat{b}_{\text{in}}(t), \tag{D2}$$

$$= -i\omega_r\hat{a}(t) - ig\hat{b}(t) - \frac{\kappa}{2}\hat{a}(t) - \sqrt{\kappa_p}\hat{b}_{\text{in}}(t), \tag{D3}$$

where $\hat{b}_{\text{in}}$ is the source term due to the drive at the input port. For a coherent drive at frequency ω_{RF}, the input mode average value is $\langle\hat{b}_{\text{in}}(t)\rangle = \bar{b}_{\text{in}}e^{-i\omega_{\text{RF}}t}$, $\langle\hat{a}(t)\rangle = \bar{a}e^{-i\omega_{\text{RF}}t}$, and $\langle\hat{b}(t)\rangle = \bar{b}e^{-i\omega_{\text{RF}}t}$, where $\bar{a}$ is the average amplitude of $\hat{a}$ at the drive frequency. We proceed in the semiclassical limit where $\langle b^\dagger b\rangle = |\bar{b}|^2$. Equation (D3) then reads

$$\bar{a} = \frac{-\sqrt{\kappa_p}\bar{b}_{\text{in}} - ig\bar{b}}{i\Delta_r + \frac{\kappa}{2}}, \tag{D4}$$

where $\Delta_r = \omega_r - \omega_{\text{RF}}$ is the detuning between the cavity and the drive signal. Then we do the same calculation to find the evolution of $\hat{b}$,

$$\bar{b} = \frac{-ig\bar{a}}{i(\Delta_0 - K|\bar{b}|^2) + \frac{\Gamma}{2}}, \tag{D5}$$

where $\Delta_0 = \omega_0 - \omega_{\text{RF}}$ is the detuning between the anharmonic oscillator and the drive signal. Injecting this into Eq. (D4) reads

$$\bar{a} = -\frac{\sqrt{\kappa_p}\bar{b}_{\text{in}}\left(i(\Delta_0 - K|\bar{b}|^2) + \frac{\Gamma}{2}\right)}{g^2 + \left(i\Delta_r + \frac{\kappa}{2}\right)\left(i\Delta_0 + \frac{\Gamma}{2}\right)}, \tag{D6}$$

$$\bar{b} = \frac{ig\sqrt{\kappa_p}\bar{b}_{\text{in}}}{g^2 + \left(i\Delta_r + \frac{\kappa}{2}\right)\left(i(\Delta_0 - K|\bar{b}|^2) + \frac{\Gamma}{2}\right)}. \tag{D7}$$

We consider that the drive signal is at the circuit frequency: $\Delta_0 = 0$ and $\Delta_r = \Delta$. Furthermore for our device $K \ll \kappa/2$, $\Gamma/2 \ll \Delta$, so that

$$\bar{a} = \frac{\sqrt{\kappa_p}\frac{\Gamma}{2}\bar{b}_{\text{in}}}{g^2 + i\Delta\frac{\Gamma}{2}}, \tag{D8}$$

$$\bar{b} = \frac{ig\sqrt{\kappa_p}\bar{b}_{\text{in}}}{g^2 + i\Delta\frac{\Gamma}{2}}. \tag{D9}$$

The average number excitations are then

$$\langle\hat{a}^\dagger\hat{a}\rangle = \frac{\kappa_p\Gamma^2}{4g^4 + \Delta^2\Gamma^2} \times \frac{P_{\text{in}}}{\hbar\omega_0}, \tag{D10}$$

$$\langle\hat{b}^\dagger\hat{b}\rangle = \frac{g^2\kappa_p}{g^4 + \Delta^2\frac{\Gamma^2}{4}} \times \frac{P_{\text{in}}}{\hbar\omega_0}. \tag{D11}$$

From room temperature measurement of the cavity, we find the coupling between the cavity mode and the port to be $\kappa_p = 0.7\,\text{MHz}$. Equation (C6) shows that fitting the linear part of $\Delta\omega(\langle\hat{b}^\dagger\hat{b}\rangle)$ gives the anharmonicity. We find the anharmonicity to be about $K = 250\,\text{kHz}$ with an uncertainty range $125\,\text{kHz} < K < 500\,\text{kHz}$, mainly due to the uncertainty on the cryostat lines attenuation.

APPENDIX E: ANHARMONIC OSCILLATOR SIMULATIONS

Rabi and Ramsey oscillations have been made using the Lindblad master equation solver of the Python's library QuTip. To simulate Rabi chevrons, we used the rotating frame Hamiltonian

$$H = \Delta\hat{b}^\dagger\hat{b} + K\hat{b}^\dagger\hat{b}^\dagger\hat{b}\hat{b} + A(\hat{b}^\dagger + \hat{b}), \tag{E1}$$

where Δ is the detuning between the drive and the anharmonic oscillator. The last term of the Hamiltonian is the drive of the oscillator, and A is the amplitude. We used $A = 0.111\,\text{rad/s}$. The Hilbert state is truncated to 120 states.

Ramsey oscillations are simulated by simulating the previous hamiltonian during a time corresponding to a $\pi/2$ pulse. We then calculate the evolution of the density matrix after the pulse using the first two terms of the Hamiltonian (E1), during a time t_{Ramsey}. We then repeat the pulse simulation on the density matrix.

In Figs. 2 and 4, the frequencies shown for the simulations are obtained by adding an offset to Δ. The offset is calculated so that the point with maximum occupation number in the simulation has the same frequency as the point with minimum phase in the measurement.

[1] A. Kringhøj, T. W. Larsen, O. Erlandsson *et al.*, Phys. Rev. Appl. **15**, 054001 (2021).

[2] M. Mergenthaler, A. Nersisyan, A. Patterson *et al.*, Phys. Rev. Appl. **15**, 064050 (2021).

[3] J. G. Kroll, W. Uilhoorn, K. L. van der Enden *et al.*, Nat. Commun. **9**, 4615 (2018).

[4] J. I-J. Wang, D. Rodan-Legrain, L. Bretheau *et al.*, Nat. Nanotechnol. **14**, 120 (2019).

[5] J. I-J. Wang, Megan A. Yamoah, Q. Li *et al.*, Nat. Mater. **21**, 398 (2022).

[6] L. Grünhaupt, M. Spiecker, D. Gusenkova *et al.*, Nat. Mater. **18**, 816 (2019).

[7] D. Rieger, S. Günzler, M. Spiecker *et al.*, Nat. Mater. **22**, 194 (2023).

[8] L. E. Bruhat, Ph.D. thesis, Ecole Normale Supérieure, 2016.

[9] H. Paik, D. I. Schuster, L. S. Bishop *et al.*, Phys. Rev. Lett. **107**, 240501 (2011).

[10] P. Winkel *et al.*, Phys. Rev. X **10**, 031032 (2020).

[11] Y. Schön, J. N. Voss, M. Wildermuth *et al.*, npj Quantum Mater. **5**, 18 (2020).

[12] N. Maleeva, L. Grünhaupt, T. Klein *et al.*, Nat. Commun. **9**, 3889 (2018).

[13] F. Friedrich, P. Winkel, K. Borisov, H. Seeger, C. Sürgers, I. M. Pop and W. Wernsdorfer, Supercond. Sci. Technol. **32**, 125008 (2019).

[14] The Rabi chevrons at 0.7 T have been measured with a larger detuning $f_{cav} - f_0$, which explains the lower phase contrast.

[15] K. Borisov, D. Rieger, P. Winkel *et al.*, Appl. Phys. Lett. **117**, 120502 (2020).

[16] N. Grønbech-Jensen and M. Cirillo, Phys. Rev. Lett. **95**, 067001 (2005).

[17] J. Claudon, F. Balestro, F. W. J. Hekking, and O. Buisson, Phys. Rev. Lett. **93**, 187003 (2004).

[18] J. Claudon, A. Zazunov, F. W. J. Hekking, and O. Buisson, Phys. Rev. B **78**, 184503 (2008).

[19] A. V. Dixit, S. Chakram, K. He *et al.*, Phys. Rev. Lett. **126**, 141302 (2021).

[20] T. Kontos, Ph.D. thesis, Orsay University, 2002.

[21] A. Blais, A. L. Grimsmo, S. M. Girvin, and A. Wallraff, Rev. Mod. Phys. **93**, 025005 (2021).